Isolating strong nanoantenna-molecule interactions by ensemble-level single-molecule detection

Lisa Saemisch[1], Matz Liebel[1] and Niek F. van Hulst[1,2,*]

[1] *ICFO-Institut de Ciencies Fotoniques, The Barcelona Institute of Science and Technology, 08860 Castelldefels, Barcelona, Spain*

[2] *ICREA-Institució Catalana de Recerca i Estudis Avançats, 08010 Barcelona, Spain*

* Corresponding author: Niek F. van Hulst ; e-mail: Niek.vanHulst@ICFO.eu

Traditionally, the nanoscale interaction between single photon emitters and plasmonic nanostructures is studied by relying on deterministic, near-perfect, nanoscale-control, either top-down or bottom-up. However, these approaches are ultra-low throughput thus rendering systematic studies difficult and time-consuming. Here, we show a highly parallelised far-field tactic, combining multiplexed super-resolution fluorescence localization microscopy and data-driven statistical analysis, to study near-field interactions between gold nanorods and single molecules, even at bulk concentrations. We demonstrate that ensemble-level single molecule detection allows separating individual emitters according to their coupling strength with tailored resonant structures, which ultimately permits the reconstruction of super-resolved 2D interaction maps around individual nanoantennas.

The advent of super-resolution techniques has revolutionised fluorescence microscopy over the past decades[1–4]. Especially the field of biology has dramatically benefited from the possibility to study structures with super-resolution microscopy (SRM). Even though it is now possible to study single molecules[5,6], cells and even small organisms[7], it is increasingly being realized that, beyond the imaging-challenge, addressing complex biological problems requires extensive data-sets[8], and high-throughput screening[9] is the next challenge to our understanding of biology. Similarly, nanophotonics research has started implementing SRM-methodologies, but the potential of large-data-driven approaches remains mostly unexplored. Here, we present a large data-set SRM approach to identify strong interactions in molecular plasmonics.

SRM in plasmonics was used first by Cang *et al*.[10] to map sub-diffraction limited features on plasmonic substrates. They interrogated a rough metallic film using the Brownian motion of freely diffusing molecules in solution and resolved surface-regions of strong fluorescence enhancement which they attributed to hotspots of approximately 15 nm in size. Their experimental interpretations were based on the assumption that determining the precise location of a fluorescence emission event is equivalent to determining an emitter's nanometric position. However, this simple assumption is based on isotropically emitting dipoles and, depending on the experimental parameters, might be only partially valid[11]. Given that far-field localizations are strongly dependent on the mere orientation of an emitter it comes as no surprise that placing a resonant nanostructure next to a molecule can dramatically alter its apparent position. This phenomenon has received considerable

attention[12] and the apparent position of molecules close to different metallic nanostructures, such as triangles[13], nanorods[14,15], nanowires[16] and more complex trimer structures[17] has been studied extensively with SRM. Unsurprisingly, all of these works show discrepancies between the true single-emitter position and its super-localized position, determined in the far field, as expected for weak emitters placed in proximity to a resonant plasmonic structure with a strong dipole-moment[18,19].

Despite these imaging problems, the combination of plasmonics with SRM holds great promise for systematically studying the interaction between individual nanostructures and fluorophores. Originally, near-field scanning optical microscopy (NSOM) has been used to study these interactions[20–23]. Albeit offering ultimate control, the experimental complexity and serial scanning of this approach dramatically limits its applicability and throughput. Less complexity offers the "*DNA-paint*" method, in which metallic nanostructures are functionalized with DNA-strands that are labelled with fluorophores[24–27]. While these fluorophores can probe the field around the nanostructure at different engineered positions, this technique is limited by the number of strands and henceforth it is not possible to probe the entire field in one experiment. On the other hand, freely diffusing molecules in solution, are able to stochastically sample the entire area around immobilised nanostructures (Figure 1a), while the complexity of the experiment is even further reduced. Here, near-field phenomena can be explored as long as sufficient number of single-molecule events, alongside their positions, are obtained. Even though offering less control than deterministic approaches or the specific local labelling, the multiplexing capabilities of plasmonic SRM are dramatic thus, in principle, allowing the simultaneous study of hundreds of individual nanostructures (Figure 1b) at all positions. Experimentally, one simply mounts the nanoantennas of interest on top of a widefield microscope, submerges the structures in a solution containing the fluorescent probe-molecules of choice (Figure 1a) and records thousands or millions of fluorescence encounters over the course of a few hours (Figure 1c)[28].

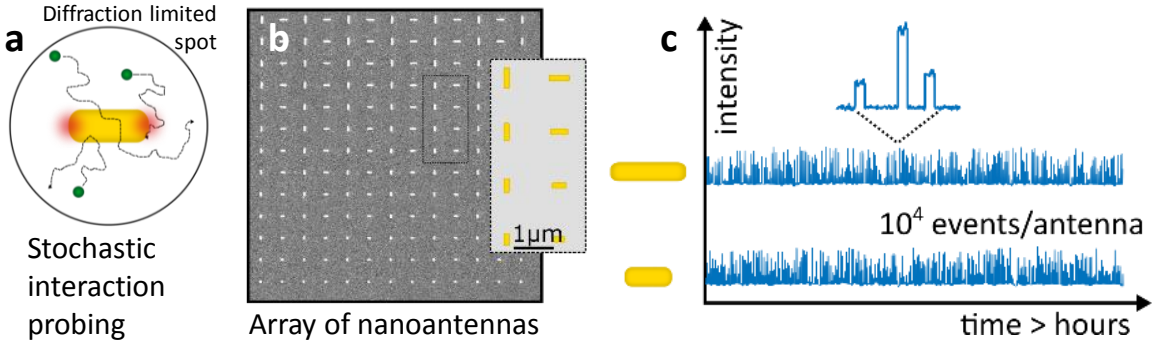

Figure 1, Stochastic nanoscale interaction mapping. a) Freely diffusing molecules stochastically scan a metallic nanostructure on nanometer scale, below the diffraction limit. b) Typical sample geometry comprised of a large array of indvidual nanoantennas (SEM image alongside schematic sample lay-out). c) Fluorescence time traces of many single molecule emission events in the vicinity of two different nanoantennas. Over the whole antenna array events are localized in parallel by wide-field imaging.

Here, we use the approach outlined above to extract molecule-antenna coupling information in a highly multiplexed fashion. We combine statistical data analysis of millions of localization-events with systematic spectral-resonance scans of plasmonic nanorods to study the spectral-overlap dependent coupling of said structures to single molecules in the near-field. Moreover, we show that rigourous statistical analysis of the localization error as well as the degree of linear polarisation (DOLP) gives direct access to the molecule-nanostructure interaction strength, allowing to reconstruct superesolved 2D interaction maps.

In order to image and study the interaction between single molecules and the said plasmonic nanostructures, we rely on a home-built total-internal-reflection (TIRF) microscope equipped with an NA 1.49 objective (Olympus APON60x) and an EM-CCD camera (Hamamatsu ImagEM X2) for wide-field detection. We plane-wave illuminate the sample of interest with 10 kW/cm^2 of linearly polarized 780 nm light under the critical angle. The objective lens collects the fluorescence emission, which is separated from residual excitation light, by a dichroic beam-splitter in combination with an 808 nm long-pass filter, and then imaged onto the EM-CCD camera at a magnification corresponding to 100 nm/pix.

A typical sample consists of electron-beam lithography-fabricated Au nanorod-arrays with varying length and orientation (Figure 1b). Nanorod-molecule interactions and their effect on the molecules' apparent far-field locations are studied by adding a solution of the laser-dye IR895, contained in *n*-BuOH, on top of the array-sample and recording stochastically occurring fluorescence events. Here, TIRF illumination is crucially important as it allows selective interaction with the individual Au nanorods at the glass/*n*-BuOH interface while limiting the volume contributing to the fluorescence background to the extent of the evanescent field, which is approximately 200 nm.

To gauge the overall experimental performance, we fabricate 100x50x58 nm Au nanorods and decrease the apex-to-apex separation between individual rods down to 50 nm (Figure 2a), which is far below the diffraction limit at the detection wavelength >808 nm. The IR895 concentration is adjusted to approximately 10 µM leading to typical fluorescence images as shown in Figure 2b. Under the experimental conditions described above and an integration time of 50 ms we observe a constant fluorescence-background from rapidly-diffusing molecules, static photoluminescence from the individual nanorods reminiscent of the SEM-image convolved with the optical point-spread-function (PSF) and stochastically varying single-molecule emission events. The two static contributions are conveniently isolated by computing a temporal running median-image[29] over batches of 400 images (Figure 2c). Subsequent subtraction of the median from the individual 400 video-frames yields essentially background-free images of the stochastically occurring emission-events of interest (Figure 2d).

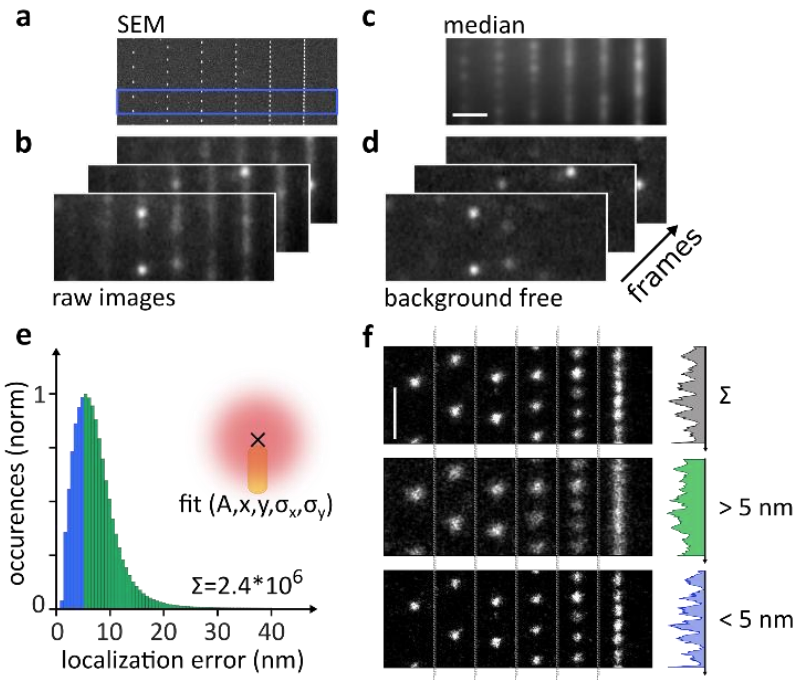

Figure 2, Proof of concept: statistical selection allows resolving closely spaced nanostructures. a) SEM image of the studied array of 100x50x58 nm nanorods, with spacing decreasing down to 50 nm. b) Representative fluorescence images as recorded on the camera after adding the *n*-BuOH solution containing IR895. c) Median luminescence background computed from 400 images. d) Background-free fluorescence images obtained by subtracting the median image from the individual frames shown in (b). Scalebar (a)-(d): 1.5 µm. e) Localization error histogram at one standard deviation of all localizations registered in the proof-of-concept experiment. Inset: Schematic of 2D Gaussian fitting of individual emission events, yielding the relevant fitting parameters *A* (amplitude), *x* and *y* (x- and y-position) and the respective localization errors σ_x and σ_y. f) Antenna positions reconstructed from stochastic single-molecule localizations using: All localizations (top), only localizations with a localization error >5 nm (center) and <5 nm (bottom). The area corresponds to the blue rectangle in a). Scalebar: 500 nm.

Temporally, essentially all emission events last less than our integration time of 50 ms with only 2% exhibiting fluorescence intensity in consecutive frames. This observation suggests that no, or only very brief, binding of the molecule to the nanostructure takes place, and that the overall "on-period" of individual molecules is considerably shorter than 50 ms. This is in good agreement with typical molecule transient times determined by fluorescent correlation spectroscopy measurements, which are on the order of tens to hundreds of microseconds, for a diffraction limited confocal volume, and even smaller for molecules diffusing through antenna hotspots[30,31].

At our IR895-concentrations typical wide-field images exhibit only few, spatially well-separated, emission events per image and their nanometric position can be determined by Gaussian fitting (Figure 2e, inset). A typical localization-error histogram calculated as $\sqrt{\sigma_x^2 + \sigma_y^2}$ for 2.4*10^6 individual single-molecule localizations, obtained after a few-hours of continuous imaging at 20 frames-per-second, is shown in Figure 2e. Qualitatively, it is reminiscent of a Boltzmann distribution with a maximum around 5 nm. In the spirit of SRM, we use the accumulated emission-events to reconstruct the underlying structure. We generate super-resolved images by summing area-normalized Gaussians with a width

corresponding to their localization-error for all detection-events (PAINT-technique[28]). Figure 2f compares different reconstructions for the Au nanorod-array using all localization-events (top), localization events with large (center) or small (bottom) localization error. A comparison of the SEM image and the reconstructed images shows good agreement between the real and the reconstructed nanorod distances (Figure 2a, highlighted area, and 2f) indicating that the fluorescence emission probability is greatly enhanced in the vicinity of the Au nanostructures. Indeed, using all detected events allows resolving individual nanorods separated by much less than the diffraction-limit. However, it is advantageous to exclusively rely on the subset of events with small localization errors in order to clearly resolve closely spaced nanorods.

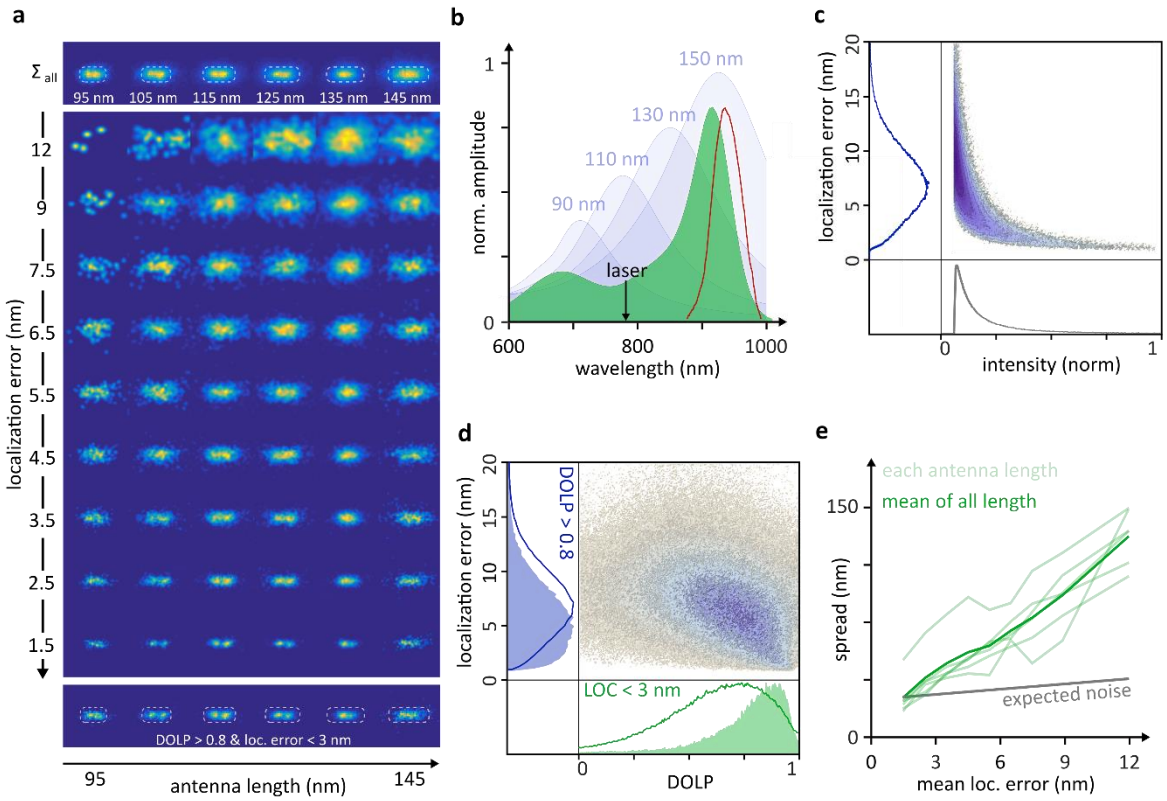

Figure 3, Role of localization error and DOLP for mapping the nanoscale interaction. a) Top: Antennas with lengths ranging from 95 to 145 nm reconstructed by relying on all detected fluorescence events. Centre: As before but by relying on data subsets with degree-of-linear-polarization (DOLP)>0.8 and decreasing localization error and, Bottom: Final reconstruction with localization errors<3 nm and DOLP>0.8. 12 individual antennas are summed per antenna length. b) IR895 absorption (green) and fluorescence (red) spectra in comparison to simulated extinction spectra of Au nanorods of different length (blue). The arrow indicates the excitation wavelength. c) Correlation between emission intensity and localization error for all detected fluorescence events alongside histogram representations. d) Correlation between the DOLP and the localization error alongside histogram representations containing the full data-set (solid line) and the localization histogram for DOLP > 0.8 (blue, filled) and a DOLP histogram for a localization error < 3 nm (green, filled). e) Mean localization error dependence of the spread around the mean antenna position for all antenna lengths compared to the expected increase estimated based on shot-noise like localization deterioration.

After these proof-of-concept experiments we now move towards systematically mapping the interactions between Au nanorods and IR895 dye-molecules by tuning the nanorod resonances. More specifically, we fabricate nanorod-arrays with antenna length ranging from 95 nm to 145 nm and a width of 58 nm. We, furthermore, equip our detection channel with a Wollaston prism to allow polarization-resolved detection parallel and perpendicular with respect to the long antenna-axis. Antenna-reconstructions obtained for s-polarized excitation and detection (along the long antenna axis), performed and analyzed analogous to the initial proof-of-concept demonstrations, are shown in Figure 3a. These reconstructions are obtained by relying on all detected fluorescence events and, furthermore, averaging 12 individual antennas for each length to reduce the effect of possible nanofabrication-imperfections. Qualitatively, all interaction maps look identical albeit a gradual increase in size with increasing nanorod length. Importantly, all reconstructed areas are smaller than the nanorod itself, as expected for experiments performed in the vicinity of resonant metallic nanostructures which are known to displace the molecular emission in the far-field[16,18,19].

Based on the absorption and emission spectrum of the previously employed laser-dye IR895 (Figure 3b) with its strongly red-shifted fluorescence band centered around 920 nm, we would expect to observe distinct signatures of both excitation- as well as emission-enhancement phenomena due to the presence of the metallic nanostructures[15]. According to simulations (Methods) the fluorescence emission maxima roughly overlaps with the resonance of the 145 nm nanorod, whereas the 780 nm excitation laser most efficiently interacts with the structures of approximately 110 nm in length. Consequently, we would expect well-separated excitation- and emission-enhancement around 110 nm and 145 nm, respectively, which should manifest themselves in distinctly different antenna-reconstructions. However, none of the anticipated effects is observed in the interaction maps.

So far, we only used the localization information of the average of all events. To extract more specific field information, we perform statistical analysis of all localization events. Figure 3c shows a correlation between the fluorescence intensity and the localization error of all fitted emission events. We observe a shot-noise like correlation with an, approximate, square-root relation between localization error and fluorescence intensity. This observation indicates that neither strong background intensities nor possible PSF-distortions, due to strong molecule-antenna coupling, affect the experimental data, as these effects would result in strong-departures from the anticipated behavior. Therefore, these parameters contain qualitatively identical information and localization-event thresholding based on either parameter should, in principle, allow isolation of strongly interacting molecules. However, our previous observations suggest that the IR895 emission events are due to molecules merely diffusing through the antenna hotspots. As a result, localization error, or intensity, based thresholding might be unable to distinguish between transiently bound molecules in a region of medium intensity, or even on bare glass, and a molecule diffusing rapidly through the high-field-intensity region of interest.

To refine the extraction of the localization events of interest we therefore introduce a second parameter, the degree of linear polarization (DOLP) computed as $DOLP=(I_s-I_p)/(I_s+I_p)$ with I_s and I_p being the fluorescence intensity of individual molecules detected in the, simultaneously

recorded, s- and p-polarized imaging channels, which are parallel and perpendicular with respect to the long antenna axis, respectively. We expect the DOLP to directly report on the antenna-molecule coupling and hence the molecules' position within the enhanced electric field around the nanorod. For molecules in close vicinity to a nanorod, the emission should be strongly polarized along the antenna axis thus resulting in the largest possible DOLP. Figure 3d shows a DOLP-localization error correlation graph, which indicates a qualitative correlation between the two values. As expected, we observe a shift towards larger DOLP values when filtering for events with small localization errors. We note that DOLP>0.8 can be readily obtained in our experiment as the molecules exhibit near-isotropic emission as they are freely diffusing in *n*-BuOH with a refractive index of n_{nBuOH}=1.4 which is close to the n=1.52 of the substrate. As a result, the commonly observed depolarization for high-NA objectives is far less pronounced[32,33].

Based on the correlation-graphs, we now attempt a refined antenna-reconstruction. We keep the DOLP>0.8 to select molecules that show considerable antenna-coupling and evaluate different localization error intervals. For the most precise localization, we observe a pronounced double-spot pattern with an approximate spot-to-spot separation of 35 nm, for shorter antennas, which merges into a single, slightly elongated spot, for longer antennas (Figure 3a, center). As we move towards higher localization errors, the features disappear, even for errors as small as 4.5 nm, which is surprising given the spot-separation of 35 nm. Intuitively, we would assume that any super-resolved feature is blurred by the localization error but a mere increase of 4.5 - 2.5 = 2.0 nm results in complete disappearance of the previously clearly resolved double-spots. To rationalize this surprising observation we quantify the deterioration by computing the spread around the mean antenna position $(\bar{x}, \bar{y})$:

$$\frac{\sum_{i=0}^{N} \sqrt{(x_i - \bar{x})^2 + (y_i - \bar{y})^2}}{N}$$

Here, we observe a dramatic departure from the expected shot-noise-limited like increase (Figure 3e) with the spread around the antenna mean increasing by 124 nm for a localization error increase of 10.5 nm. From a SRM point-of-view, this observation might appear surprising. However, the electric field distribution around a nanoantenna is not a structure with a well-defined, binary, shape but rather a function with boundaries that depend on the intensity-enhancement and interaction strength with the molecular probes. A poorly-localized molecule is therefore more likely to be further away from the nanorod than a well-localized one thus increasing the absolute area that is sampled around the antenna. This localization error-based sampling space results in a rapid loss of the high electric-field-intensity information. Based on these observations we attempt the "ideal" antenna intensity reconstruction based on all localization events with a DOLP>0.8 and a localization error <3 nm (Figure 3a (bottom)), which shows a gradual transition from a double to a single spot upon varying the antenna resonance.

To rationalize these experimental observations, we perform finite-difference-time-domain (FDTD) simulations using the Lumerical solver (Methods). To this end, we simulate the radiation patterns of x- and y-oriented dipoles (molecules) at different positions around the nanorod and then generate far field images reflecting our experimental imaging system. The respective images are processed analogous to the experimental data. Ultimately, we obtain

a simulated reconstructed image where the intensity of each dipole emitter corresponds to the excitation field intensity of the nanorod at the emitters' location. Figure 4a shows a comparison between the experimentally obtained results for 115, 135 and 145 nm long nanorods and the corresponding simulation. Here, the three lengths show qualitatively the transition from excitation to emission enhancement. As in the experiment, we observe a the pattern change with most of the fluorescence intensity being localized in the center of the antenna once its resonance overlaps with the molecular emission spectrum which is in good agreement with previously reported experimental studies and simulations[14,34]. The slight deviations between our experimental data and the simulations are most likely due to the insufficient quality of the experimental data as well as the crude modelling of the antenna-molecule coupling strength. Here, we restrict our model two a single 2D plane, located 5 nm above the sample-substrate, of molecule-nanorod interactions rather than the full 3D volume around the antenna. Additionally, we model the ideal shape of the nanorod after fabrication, where surface irregularities and slight deformations are ignored, an ideal scenario that we tried to reproduce by summing a total of 12 individual antennas per length. Especially for excitation wavelengths blue-shifted with respect to an antenna resonance the excitation enhancement is generally reduced[35,36] thus complicating the experiment considerably, a fact that manifests itself in the reduced data quality of the 135 and 145 nm data as compared to the data obtained with the red-shifted excitation of the 115 nm antenna.

To conclude the data-driven mapping of molecule-antenna coupling strength we now turn our attention to the molecular events detected with emission polarization perpendicular with respect to the excitation polarization as well as the antenna-resonance axis. Contrary to the coupling case in Figure 4a, molecular events detected in this "cross-polarization" do not couple to the long axis of the nanoantenna – hence we are able to separate the coupling and non-coupling events around the same nanoantenna. Based on the strong DOLP bias of our experiment (Figure 3d) and the unfavorable excitation and emission enhancement of perpendicularly-oriented molecules we expect few emission events with little-to-no intensity in the cross-polarized imaging channel. The large amount of localization events recorded nevertheless allows us to analyze the electric fields governing emission through this channel. Figure 4b shows an emission-intensity reconstruction of the 115 and 125 nm nanorods for 12 summed antennas based on approximately 1100 events with a localization error < 7.1 nm and DOLP < -0.4. The patterns are both reminiscent of the cloverleaf-like PSFs previously observed as far-field emission patterns of individual emitters positioned above a nanowire[37]. However, our reconstruction is based on post-detection reconstruction, which incorporates Gaussian fitting which necessarily results in a complete loss of PSF shape-information. To rationalize our observation, we simulate the y-component of the electric field present around a 125 nm nanorod, under far-field TIRF-excitation with light polarized along the long axis of the nanorod. The near-perfect agreement between experimentally observed fluorescence localizations and theoretically predicted excitation intensity suggests that we purely probe the y-component of the electric antenna field without any interaction of molecule and nanoantenna. The cloverleaf pattern does not depend on the nanorod length. Our results confirm the findings obtained by direct near field imaging of the vectorial nanorod fields with a scanning antenna tip[20].

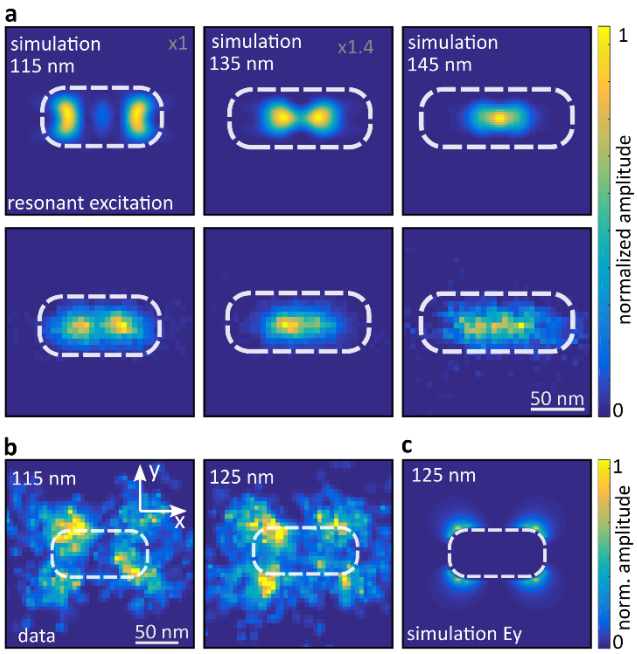

Figure 4, Comparison between simulations and experimental observations.
(a) (top) Localization maps from FDTD simulations for 115, 135 and 145 nm antennas compared to (bottom) experimental intensity distributions, reconstructed by applying a threshold with localization error < 4 nm and DOLP > 0.8. (b) Experimentally reconstructed intensity distribution for cross-polarized localizations with localization error < 7.1 nm and DOLP < -0.4 for 115 and 125 nm antennas, in comparison to (c) a FDTD simulation of the y-component of the electric field around the nanoantenna.

In summary, we constructed a wide-field TIRF microscope and employed arrays of nanoantennas with increasing length that resonantly interact with individual emitters at both excitation and emission frequencies. Depending on the antenna length, either emission- or excitation-induced effects resulted in remarkable changes in the observed super-resolved intensity reconstructions. Instead of concentrating on these now well-understood, and widely studied, discrepancies between expected and measured electric field distributions, we instead emphasize the true strength of wide-field super-resolution mapping of plasmonic structures: the possibility to perform highly-parallelized high-throughput experiments in combination with thorough statistical analysis. While most of nanoplasmonics relies on point-scanning - or confocal - observations, which are intrinsically throughput-limited, the “PAINT”-technique yields millions of single-molecule observations while, simultaneously, being considerably easier to experimentally implement. As a result, intensity and polarization measurements allow us to isolate a small subset of strongly-coupled single molecules from an enormous number of less-coupled emitters and background, purely based on statistical analysis that relies on physically meaningful expectations. Based on this analysis we resolved the expected double-spot excitation enhancement pattern present around the antenna-apexes, which would have remained unresolved if statistical filtering would not have been applied. Furthermore, we were able to resolve the E_y-component of the electric field in a cross-polarization analysis, by isolating the few events that did not couple to the long axis of the nanoantenna.

Our approach highlights that single-molecule based approaches are extremely powerful when conducted at ensemble-level detection levels. Here, rarely occurring events, such as the strong coupling of an individual molecule to a plasmonic structure, can be identified with statistical significance. Importantly, such observations are impossible with ensemble-based techniques and would have most likely been discarded as artefacts in traditional single emitter experiments, which often draw conclusions based on a few tens of observations. Ensemble-level single molecule spectroscopy eliminates these problems and allows confident identification and study of physical phenomena based on rigorous statistical analysis.

Overall, this is a robust method for finding specific and rare cases of stronger interaction out of an ensemble of many random occurrences. We can imagine an implementation e.g. in a bio-analytical laboratory, where a simple post-processing thresholding program will reveal specific interactions. Compared to the serial near-field scanning antenna approach, our parallel experiment is considerably easier to implement and execute. In the near future, our method might be applied for subwavelength sensing in future mini CMOS cameras. Finally, the occurrence of light re-localisation provides an interesting concept for light concentration applications in general, such as in solar light harvesting.

We are currently extending our methodology towards highly-multiplexed imaging incorporating simultaneous position, polarization and spectral detection. These extended capabilities, in combination with the statistical analysis introduced here, will allow us to observe the transition from uncoupled to strongly coupled emitters as they approach resonant plasmonic nanostructures.

Methods

FDTD calculations (I) – Molecule and antenna interaction. The FDTD calculations are performed using the Lumerical FDTD solver. In all calculations, the nanostructure is modelled as being supported on top of a glass substrate with a refractive index of 1.5 and being surrounded by a medium with a refractive index of 1.4, corresponding to the refractive index of *n*-BuOH. The nanostructure is a nanorod with a constant width of 58 nm and height of 50 nm, and a length of 115 nm or 135 nm, on top of a 2 nm thick titanium layer. We simulate the radiation patters of X and Y oriented dipoles at a fixed height of 5 nm above the glass substrate at different positions around the nanorod and collect the electric fields 10 nm below the substrate. We then perform a Fourier transformation to access the far field. Only collection angles smaller than the critical angle defined by our numerical aperture of 1.49 are retained. After Fourier filtering the radiation pattern is propagated back into the image plane and fitted analogous to the experimentally obtained data. A 2D Gaussian is then plotted at each obtained x-/y-position using a width of 6 nm at one standard deviation and an intensity corresponding to the excitation intensity of the nanorod at the original location of the dipole emitter – here we match the two dipole orientations with the two components of the excitation field (E_x and E_y).

We model the ideal shape of the nanorod after fabrication, where surface irregularities and slight deformations are ignored, an ideal scenario that we tried to reproduce by summing a total of 12 individual antennas per length.

FDTD calculations (II) - Nanorod resonances. To simulate the nanorod resonances in TIRF excitation and submerged in butanol, we used the total-field-scattered-field source in order to quantify absorption and transmission of the plasmonic structure at different wavelengths.

Sample preparation. We use electron-beam lithography to fabricate the sample. To this end, we evaporate a 2 nm titanium layer followed by a 50 nm gold layer. We spin-coat 150 µm of the resist ARN7500.08 on top of the gold at 8000 RPM for 60 s. After electron-beam exposure and development (ARN300, diluted 4:1 with water), reactive Ion etching is employed with an Oxford Instruments Plasmalab System leaving only the Au nanorods on top of the coverglass.

Acknowledgements

Authors acknowledge support by the Ministry of Science, Innovation and Universities (MCIU/AEI: BES-2016-078727, RTI2018-099957-J-I00 and PGC2018-096875-B-I00). N.F.v.H. acknowledges the financial support by the European Commission (ERC Advanced Grant 670949-LightNet), Ministry of Economy ("Severo Ochoa" program for Centers of Excellence in R&D SEV-2015-0522 and Plan Nacional FIS2015-69258-P), the Catalan AGAUR (2017SGR1369), Fundació Privada Cellex, Fundació Privada Mir-Puig, and Generalitat de Catalunya through the CERCA program. Furthermore the authors thank G. Calbris for help with the FDTD simulations.

1. Betzig, E. *et al.* Imaging Intracellular Fluorescent Proteins at Nanometer Resolution. *Science* **313**, 1642–1645 (2006).
2. Hell, S. W. & Wichmann, J. Breaking the diffraction resolution limit by stimulated emission : stimulated-emission-depletion fluorescence microscopy. *Opt. Lett.* **19**, 780–782 (1994).
3. Hess, S. T., Girirajan, T. P. K. & Mason, M. D. Ultra-High Resolution Imaging by Fluorescence Photoactivation Localization Microscopy. *Biophys. J.* **91**, 4258–4272 (2006).
4. Rust, M. J., Bates, M. & Zhuang, X. Sub-diffraction-limit imaging by stochastic optical reconstruction microscopy (STORM). *Nat. Methods* **3**, 793–795 (2006).
5. Stipe, B. C., Rezaei, M. A. & Ho, W. Single-Molecule Vibrational Spectroscopy and Microscopy. *Science* **280**, 1732–1753 (1998).
6. Kneipp, K. *et al.* Single Molecule Detection Using Surface-Enhanced Raman Scattering (SERS). *Phys. Rev. Lett* **78**, 1667–1670 (1997).
7. Liu, T. L. *et al.* Observing the cell in its native state: Imaging subcellular dynamics in multicellular organisms. *Science* **360**, 1–13 (2018).
8. Boettiger, A. N. *et al.* Super-resolution imaging reveals distinct chromatin folding for different epigenetic states. *Nature* **529**, 418–422 (2016).
9. Beghin, A. *et al.* Localization-based super-resolution imaging meets high-content screening. *Nat. Methods* **14**, 1184–1190 (2017).
10. Cang, H. *et al.* Probing the electromagnetic field of a 15-nanometre hotspot by single molecule imaging. *Nature* **469**, 385–388 (2011).

11. Backlund, M. P., Lew, M. D., Backer, A. S., Sahl, S. J. & Moerner, W. E. The Role of Molecular Dipole Orientation in Single- Molecule Fluorescence Microscopy and Implications for Super-Resolution Imaging. *ChemPhysChem* **15**, 587–599 (2014). doi:10.1002/cphc.201300880

12. Willets, K. A., Wilson, A. J., Sundaresan, V. & Joshi, P. B. Super-Resolution Imaging and Plasmonics. *Chem. Rev.* **117**, 7538-7582 (2017). doi:10.1021/acs.chemrev.6b00547

13. Wertz, E. A., Isaacoff, B. P. & Biteen, J. S. Wavelength-Dependent Super-resolution Images of Dye Molecules Coupled to Plasmonic Nanotriangles. *ACS Photonics* **3**, 1733–1740 (2016).

14. Su, L. *et al.* Super-resolution Localization and Defocused Fluorescence Microscopy on Resonantly Coupled Single-Molecule, Single-Nanorod Hybrids. *ACS Nano* **10**, 2455–2466 (2016).

15. Blythe, K. L., Titus, E. J. & Willets, K. A. Effects of Tuning Fluorophore Density, Identity, and Spacing on Reconstructed Images in Super-Resolution Imaging of Fluorophore- Labeled Gold Nanorods. *J. Phys. Chem. C* **119**, 28099–28110 (2015).

16. Ropp, C. *et al.* Nanoscale probing of image-dipole interactions in a metallic nanostructure. *Nat. Commun.* **6**, 6558 (2015).

17. Mack, D. L. *et al.* Decoupling absorption and emission processes in super-resolution localization of emitters in a plasmonic hotspot. *Nat. Commun.* **8**, (2017).

18. Raab, M., Vietz, C., Stefani, F. D., Acuna, G. P. & Tinnefeld, P. Shifting molecular localization by plasmonic coupling in a single-molecule mirage. *Nat. Commun.* **8**, 13966 (2017).

19. Lim, K. *et al.* Nanostructure-Induced Distortion in Single-Emitter Microscopy. *Nano Lett.* **16**, 5415–5419 (2016).

20. Kühn, S., Hakanson, U., Rogobete, L. & Sandoghdar, V. Enhancement of Single-Molecule Fluorescence Using a Gold Nanoparticle as an Optical Nanoantenna. *Phys. Rev. Lett.* **97**, 017402 (2006).

21. Singh, A., Calbris, G. & van Hulst, N. F. Vectorial Nanoscale Mapping of Optical Antenna Fields by Single Molecule Dipoles. *Nano Lett.* **14**, 4715–4723 (2014).

22. Singh, A., De Roque, P. M., Calbris, G., Hugall, J. T. & Van Hulst, N. F. Nanoscale Mapping and Control of Antenna-Coupling Strength for Bright Single Photon Sources. *Nano Lett.* **18**, 2538–2544 (2018).

23. Mivelle, M., Zanten, T. S. Van, Neumann, L., van Hulst, N. F. & Garcia-Parajo, M. F. Ultrabright Bowtie Nanoaperture Antenna Probes Studied by Single Molecule Fluorescence. *Nano Lett.* **12**, 5972–5978 (2012).

24. Jungmann, R. *et al.* Super-Resolution Microscopy by Fluorescence Imaging of Transient Binding on DNA Origami. *Nano Lett.* **10**, 4756–4761 (2010).

25. Simoncelli, S., Li, Y. & Maier, S. A. Imaging Plasmon Hybridization of Fano Resonances via Hot-Electron-Mediated Absorption Mapping. *Nano Lett.* **18**, 3400–3406 (2018).

26. Simoncelli, S., Li, Y., Cortés, E. & Maier, S. A. Nanoscale Control of Molecular Self-Assembly Induced by Plasmonic Hot-Electron Dynamics. *ACS Nano* **12**, 2184–2192 (2018).

27. Taylor, A., Verhoef, R., Beuwer, M., Wang, Y. & Zijlstra, P. All-Optical Imaging of Gold Nanoparticle Geometry Using Super- Resolution Microscopy. *J. Phys. Chem. C* **122**, 2336–2342 (2018).

28. Sharonov, A. & Hochstrasser, R. M. Wide-field subdiffraction imaging by accumulated binding of diffusing probes. *Proc. Natl. Acad. Sci. U.S.A.* **103**, 18911–18916 (2006).

29. McFarlane, N. J. B. & Schofield, C. P. Segmentation and tracking of piglets in images. *Mach. Vis. Appl.* **8**, 187–193 (1995).

30. Flauraud, V. *et al.* In-Plane Plasmonic Antenna Arrays with Surface Nanogaps for Giant Fluorescence Enhancement. *Nano Lett.* **17**, 1703–1710 (2017).

31. Punj, D. *et al.* A plasmonic ' antenna-in-box ' platform for enhanced single-molecule analysis at micromolar concentrations. *Nat. Nanotechnol.* **8**, 512–516 (2013).

32. Taminiau, T. H., Stefani, F. D., Segerink, F. B. & van Hulst, N. F. Optical antennas direct single-molecule emission. *Nat. Photonics* **2**, 234–237 (2008).

33. Axelrod, D. Carbocyanine Dye Orientation in Red Cell Membrane Studied by Microscopic Fluorescence Polarization. *Biophys. J.* **26**, 557–574 (1979).

34. De Silva Indrasekara, A. S. *et al.* Optimization of Spectral and Spatial Conditions to Improve Super-Resolution Imaging of Plasmonic Nanoparticles. *J. Phys. Chem. Lett.* **8**, 299–306 (2017).

35. Thomas, M., Greffet, J.-J., Carminati, R. & Arias-Gonzales, J. R. Single-molecule spontaneous emission close to absorbing nanostructures. *Appl. Phys. Lett.* **85**, 3863–3865 (2004).

36. Anger, P., Bharadwaj, P. & Novotny, L. Enhancement and Quenching of Single-Molecule Fluorescence. *Phys. Rev. Lett.* **96**, 113002 (2006).

37. Su, L. *et al.* Visualization of molecular fluorescence point spread functions via remote excitation switching fluorescence microscopy. *Nat. Commun.* **6**, 6287 (2015).